nature materials

Article

https://doi.org/10.1038/s41563-023-01785-w

High-quality nanocavities through multimodal confinement of hyperbolic polaritons in hexagonal boron nitride

Received: 9 October 2022

Accepted: 5 December 2023

Published online: 06 February 2024



Hanan Herzig Sheinfux © ^{1,2}, Lorenzo Orsini © ¹, Minwoo Jung © ³, Iacopo Torre © ¹, Matteo Ceccanti ¹, Simone Marconi ¹, Rinu Maniyara © ¹, David Barcons Ruiz ¹, Alexander Hötger ⁴, Ricardo Bertini © ¹, Sebastián Castilla © ¹, Niels C. H. Hesp © ¹, Eli Janzen ⁵, Alexander Holleitner ⁴, Valerio Pruneri © ^{1,6}, James H. Edgar © ⁵, Gennady Shvets ⁷ & Frank H. L. Koppens © ^{1,6}

Compressing light into nanocavities substantially enhances light-matter interactions, which has been a major driver for nanostructured materials research. However, extreme confinement generally comes at the cost of absorption and low resonator quality factors. Here we suggest an alternative optical multimodal confinement mechanism, unlocking the potential of hyperbolic phonon polaritons in isotopically pure hexagonal boron nitride. We produce deep-subwavelength cavities and demonstrate several orders of magnitude improvement in confinement, with estimated Purcell factors exceeding 10⁸ and quality factors in the 50–480 range, values approaching the intrinsic quality factor of hexagonal boron nitride polaritons. Intriguingly, the quality factors we obtain exceed the maximum predicted by impedance-mismatch considerations, indicating that confinement is boosted by higher-order modes. We expect that our multimodal approach to nanoscale polariton manipulation will have far-reaching implications for ultrastrong light-matter interactions, mid-infrared nonlinear optics and nanoscale sensors.

Confining light into a deep-subwavelength volume has been a major driver of nanophotonics research over the last few decades. Innovations in nanocavity design¹ allow light to be confined to extremely subwavelength volumes, enabling even single emitters to be strongly coupled to cavity polaritons²-⁴. Likewise, nanocavity coupling strengths can become so large that they reach the onset of ultrastrong-coupling⁵ and deep-coupling⁶ regimes, where bound states entangle with virtual excitations^{7,8}, challenging the basic tenet of perturbative light–matter

interactions. Moreover, cavities with strongly spatially varying fields are expected to induce super-radiant quantum phases 9 . Therefore, creating cavities with deep-wavelength mode volume is the key to progress in fundamental physics as well as in a range of applications such as quantum chemistry and the manipulation of matter $^{10-14}$.

However, compressing light to the nanometric scale typically comes at a cost: high absorption losses, which plague all existing nanocavity designs and are intrinsic with metal- or semimetal-based cavities.

¹ICFO-Institut de Ciencies Fotoniques, The Barcelona Institute of Science and Technology, Castelldefels (Barcelona), Spain. ²Department of Physics, Bar-Ilan University, Ramat Gan, Israel. ³Department of Physics, Cornell University, Ithaca, NY, USA. ⁴Walter Schottky Institut and Physik Department, Technische Universitat Munchen, Garching, Germany. ⁵Tim Taylor Department of Chemical Engineering, Kansas State University, Durland Hall, Manhattan, KS, USA. ⁶ICREA—Institució Catalana de Recerca i Estudis Avançats, Barcelona, Spain. ⁷School of Applied and Engineering Physics, Cornell University, Ithaca, NY, USA. ⊠e-mail: frank.koppens@icfo.eu

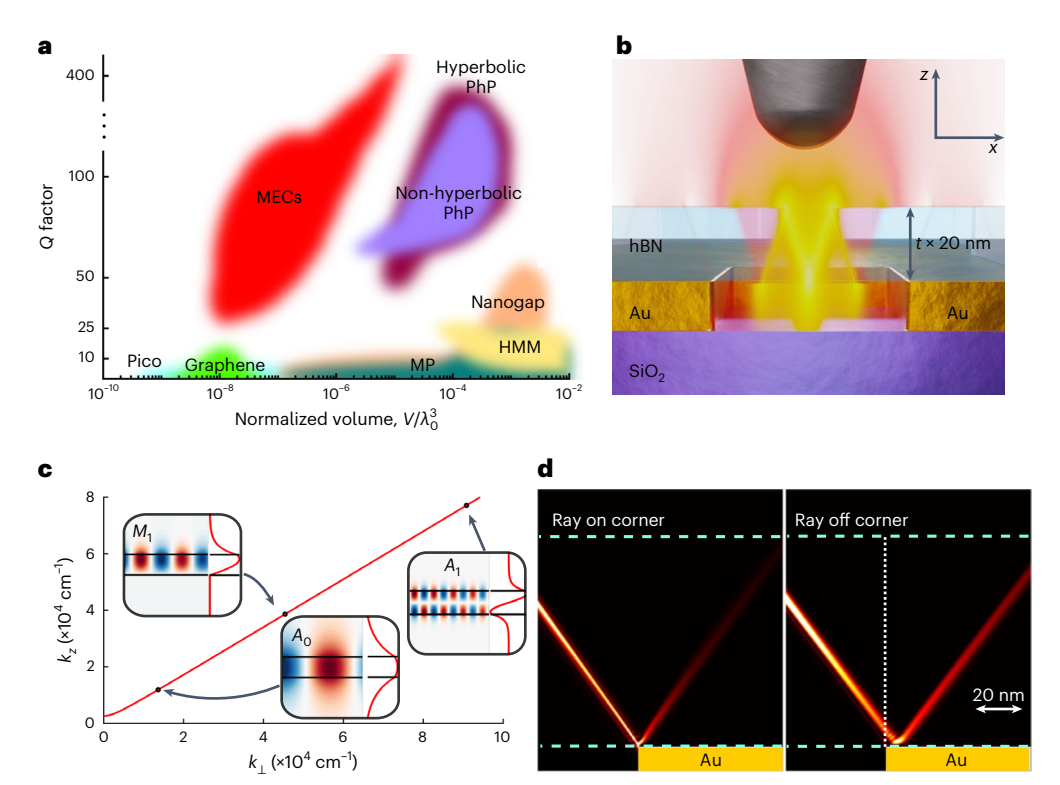


Fig. 1 | **Nanocavities in the literature and MECs. a**, Survey of the Q factor and normalized cavity volume (normalized by the vacuum photon volume) for various types of cavities, based on tabulated data (Supplementary Section 1). The coloured areas correspond to different cavity types: picocavities 2,3 (pico), nanogap plasmon polaritons 15,16 (nanogap), graphene plasmon polaritons $^{17-20}$ (graphene), metallic particles 21,22 (MP), hyperbolic metamaterials 23,24 (HMM), non-hyperbolic 25,26 and hyperbolic $^{27-35,41}$ phonon polaritons (PhP), and the multimodal enhanced cavities (MECs) studied here. Generally, cavities with V below V show low V factors, typically below 10 and always below 20 (Supplementary Section 1). **b**, Schematic of the cross-section of an MEC cavity, superimposed with the simulated electric-field amplitude (in-plane component) of a resonant cavity, showing the ray-like characteristics of the standing wave inside the cavity. The simulation aspect ratio is adjusted for clarity and the range of yellow colour indicates the field maximum. **c**, Isofrequency line in momentum space, with the PhP eigenmodes V (in suspended hBN) and V (on a metallic

substrate) indicated by the black dots (for experimental parameters, similar to device N1). The insets show the calculated electric-field distribution and profile of these modes (Supplementary Section 2.1 provides the derivation). Additional higher-momentum modes (not shown in the figure) are involved in the multimodal reflection process. **d**, Simulated intensity profile of a multimodal ray propagating inside an hBN flake (edges indicated by cyan lines) when it is incident on a single metallic corner or incident -10 nm after the corner (the virtual interface of reflection is indicated by the dashed white line). Due to the reduced overlap with the modes over the metal, the ray incident on the corner reflects strongly and in an anomalous way such that it continues propagating back to the left (Supplementary Video 1). The ray incident after the corner shows the usual propagation to the right. The dipole of the ray is situated outside (to the left) and is not shown to avoid colour saturation (Supplementary Section 4.3). The same colour map is used in both plots, where a brighter colour corresponds to a higher intensity.

Figure 1a visually summarizes the state of the art in nanocavity research $^{15-35}$ and shows that cavity performance progressively degrades for $V<10^{-4}\lambda_0^3$, where λ_0 is the vacuum wavelength. Similarly, on the absolute scale, cavity performance drops when the cavity dimensions drop below 100 nm. Virtually, all polaritonic cavities on that size scale show low quality (Q) factors, corresponding to a lifetime of just one or two optical periods. Moreover, due to the slow group velocity typical to light at the nanoscale, light does not complete a single cycle inside a nanocavity before losing most of its power 36 (Supplementary Section 1), in stark contrast to the common intuitive conception of cavities as multi-bounce resonators. This appears to be an intrinsic challenge for plasmonic nanocavities, which motivates the pursuit of a different material platform.

Alternative materials are those that host hyperbolic phonon polaritons (PhPs). Of specific interest are crystals such as hexagonal boron nitride (hBN) or MoO₃ as they support PhPs in their Reststrahlen bands with very high momenta and relatively low losses^{33–39}. For example, extreme confinement can be achieved with hBN nanotubes⁴⁰ where whispering-gallery modes can attain extremely high momentum $(\lambda_p \approx \lambda_0/500 \text{ polariton wavelength})$ and $Q \approx 100$. More commonly, PhP cavities are formed out of thin hBN flakes by etching hBN^{27–33}. The cavities can achieve Q > 200 and have sizes on the order of ~300 nm

 $(\lambda_p \approx \lambda_0/30)$, and these cavities can be passively tuned by varying their dielectric environment⁴¹. Intrinsically, isotopically pure hBN cavities could attain extremely small volumes of the nanometre scale combined with very high Q factors approaching the intrinsic PhP Q factor of 800. However, in practice, nanoscale material damage (a combination of surface roughness and surface degradation) is inevitable in conventional directly patterned (etched) cavities and—to the best of our knowledge—leads to increased absorption and surface scattering, which restricts the attainable size and Q factor.

It is, therefore, enticing to identify a different way to confine polaritons, to harness the full potential of hyperbolic materials. However, to do so, two major hurdles must be overcome: first, field confinement in the cavity by momentum mismatch alone is inefficient, as a substantial amount of the energy leaks out of the cavity. Second, being a hyperbolic material, hBN supports many (in principle, infinite) PhP modes³³. Ordinarily, these additional modes are expected to provide additional leakage channels, further degrading the retention time of light in the cavity.

Here we turn these challenges into opportunities by utilizing the hyperbolic nature of long-lived PhPs in isotopically pure hBN, thereby achieving the previously unattainable fusion of high Q factors with ultrasmall modal volumes. Uniquely, optical confinement in our

cavities is enhanced rather than reduced by the additional higher-order modes, owing to a unique multimodal reflection enhancement mechanism. Our experimental observations are made with scattering-type near-field optical microscopy (SNOM) $^{42-44}$ and directly demonstrate the previously unattainable Q > 100 in ultracompact cavities on the 100-nm-size scale. These cavities are orders of magnitude smaller than any comparable existing high-Q-factor polaritonic cavity. At the same time, we also demonstrate that larger nanocavities show Q in the 400-500 range, approaching the intrinsic PhP Q factor, and higher than any previously reported value for polaritonic nanocavities, including directly defined hBN cavities 31 . Moreover, the observed Q factors can exceed the maximum single-mode Q factor and are explained in terms of multimodal reflection enhancement.

The general design of our multimodal enhanced cavity (MEC) is shown in Fig. 1b and consists of a sharply defined hole in a gold film covered by a thin hBN flake. The hBN acts as a slab waveguide for PhPs, with the dispersion of PhP modes indirectly affected by the permittivity of the environment (Supplementary Section 2.1). Above the hole, the first PhP mode A_0 has a much smaller momentum (longer wavelength) than the PhP modes M_1 , M_2 ... of hBN on gold (Fig. 1c). Light is confined in hBN in the region above the hole, through a combination of two mechanisms. First, by impedance mismatch between the modes inside and outside. Second, by a multimodal mechanism, unique to hyperbolic media, which can be understood as follows.

A dipole above the hBN slab can excite multiple modes and the interference between these modes produces a sharply localized nanoray^{45,46} with a width of just a few nanometres. This ray can be reflected at the top and bottom surfaces of the flake, producing a zig-zag motion. When this ray is incident on a sharp metallic corner (Fig. 1d), it experiences strong reflection to the left such that it propagates back into the original ray path (Supplementary Video 1). This is due to the diminished overlap between the ray with the $M_1, M_2...$ modes on the metallic substrate (Supplementary Section 4.3 provides the details), and is therefore earmarked as a multimodal reflection process. On the contrary, if the beam misses the corner, it is mirrored from the bottom surface as usual and shows almost perfect transmission to the right. Further hints of the role of multimodal interference are apparent in the simulated cavity-mode profile (Fig. 1b and Supplementary Section 4.2), which shows ray-like features that result from the combination of high-order modes. We discuss the multimodal reflection enhancement further down, evaluating the relative strength of the two abovementioned mechanisms.

Experimentally, our MECs are made by milling holes in an ultraflat layer of gold, using a focused-ion-beam microscope (FIB) with extreme resolution of a few nanometres. This is essential, as the sharpness of the metal corner governs the efficiency of the ray reflection amplitude. We transferred an isotopically pure ¹¹B hBN flake on top of the milled pattern (Methods and Supplementary Section 3). Since the hBN flake is not directly milled nor processed in any way, it maintains very low PhP losses, typical for pristine isotopically pure hBN flakes^{38,39}. Below, we consider four cavity sets: N1 and N2, both of which are milled by Ne-based FIB, comprising an hBN flake with a thickness of 25 and 3 nm, respectively; and H1 and H2, made with a He-based FIB having a thickness of 3 and 32 nm, respectively.

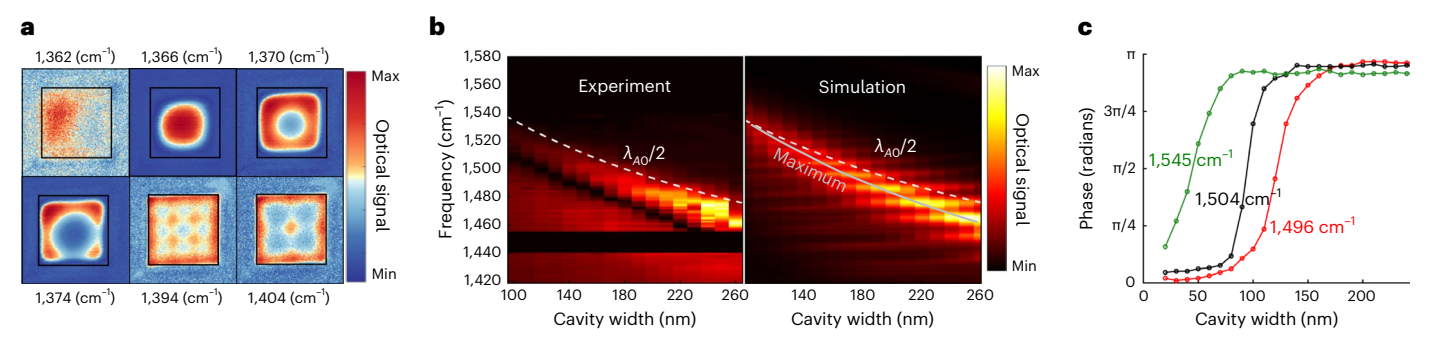
The near-field SNOM signal (fourth-harmonic homodyne), measured for a fixed frequency f, from a representative $600 \times 600 \text{ nm}^2$ square cavity in the H1 set is shown in Fig. 2a for a number of frequencies. This signal is directly related to the spatial distribution of the (projected) local density of states (Supplementary Section 5.1) and shows a clear evolution with frequency. The mode profile suggests that this is the lowest-order cavity mode and the rapid rate of change with frequency indicates a large Q factor. Repeating this measurement for a set of cavities with different widths (in cavity set N1), we obtain the data shown in Fig. 2b, which shows the normalized near-field signal in the middle of the cavity as a function of frequency and cavity width.

The experiments closely agree with the full Maxwell finite-element simulations (Supplementary Section 4.1). However, in particular, the width of the cavities is slightly shifted relative to $\lambda_{A_0}/2$, half the in-plane wavelength of A_0 . This suggests a possible deviation from the simple impedance-mismatch scenario (for example, a phase acquired on reflection).

As the cavity width shrinks, the signal strength becomes weaker since the near-field microscope picks up less signal, but both experimental and simulated resonances (Fig. 2b) remain narrow, suggesting that the Q factor of the cavities does not degrade. In fact, the signal reduction witnessed in the experiment is primarily due to the tip (mechanically) drifting away from the cavity during the frequency sweep. To circumvent this drift problem, we apply pseudoheterodyne (PsHet) SNOM measurement at a fixed frequency to obtain the complex amplitude and phase. From these data, we extracted the optical phase as a function of the cavity width (Fig. 2c and Supplementary Section 5.5). The measured data show a clear π -phase jump, as expected when changing a critical parameter across a resonance. This phase response in cavity set N1 can be clearly identified and quantified for cavities down to 60×60 nm². To shrink the cavity size further, we turn to cavity set N2, where the hBN is even thinner (3 nm) and where even smaller cavities are made. These very small cavities show a weaker signal, which complicates the measurement, but we can nevertheless identify the cavity response down to a cavity size of $23 \times 23 \times 3$ nm³.

This raises the question: what is the smallest cavity size that can be produced using our approach? Remarkably, the limit of the smallest cavity size seems to not be technical (for example, fabrication capability) or fundamental (for example, losses or spatial non-locality in the PhP dispersion). Rather, the limit to cavity size is determined by our ability to measure such small cavities with the near-field microscope. The smallest cavities we measured are smaller than the diameter of the SNOM tip, and the wavelength associated with the PhPs in our cavities is already more than 200 times smaller than the vacuum wavelength, which is the highest compression seen in an infrared near-field measurement³⁸ (we note that the evidence for even stronger compression appears in monolayer hBN, using electron microscopy⁴⁷). With such extreme wavelength contraction and considering that the area of the tip is several times larger than the cavity, it is normally expected that the coupling efficiency would be extremely low. It is, thus, remarkable that any near-field response is observed in our experiments.

Next, we quantify the O factor for a range of cavity sizes, taken from different cavity sets and using different methods (Fig. 3a; Supplementary Section 5 provides a detailed explanation). We find that Q factors above 50 are typical for cavities with volumes on the order of $V = 2 \times 10^5 \text{ to } 10^6 \text{ nm}^3$. Peak confinement values are on the order of $Q \approx 90$ for $V \approx 50 \times 50 \times 25 \text{ nm}^3 \text{ (N1) to } Q \approx 125 \text{ for } V \approx 60 \times 60 \times 3 \text{ nm}^3 \text{ (N2) and}$ $Q \approx 75$ for $V \approx 90 \times 90 \times 33$ nm³ (H2). When normalized by the vacuum-mode volume, that is, $V_0 = \lambda_0^3$, this yields volumes on the order of 3×10^{-7} to $4 \times 10^{-8} \lambda_0^{-3}$. In both absolute and wavelength-normalized terms, these volumes are orders of magnitude smaller than the volume of any previous cavity of comparable mode quality. Furthermore, in relatively wide cavities, such as the $V \approx 600 \times 600 \times 3 \text{ nm}^3$ cavity (in H1), the spectral response becomes exceedingly sharp (Fig. 3b) and fitting yields a Q factor well above 400 (black dash-dot line is the best fit with $Q \approx 480$). The quality factor achieved exceeds that previously obtained with any PhP cavity³¹, nearing the intrinsic, absorption-limited value of approximately Q~650 (assuming perfect reflections), for the specific boron isotope under consideration. Based on a semi-analytical calculation of the loss function in a trench cavity⁴⁸, we find that the modes are strongly localized in the cavity, suggesting that the mode volumes should be comparable to the cavity volume. We note that the smallest cavities, including the $23 \times 23 \times 3$ nm³ ($5 \times 10^{-9} \lambda_0^3$) cavity studied above, also appear to possess substantial Q factors. However, due to the weaker signal associated with those small cavities, the error magnitude is much larger, preventing us from accurately assessing the Q factor.



 $\label{eq:Fig.2} \textbf{PREAR_INDER_IND$

and cavity size (cavity set N1). The dashed white line shows the expected first-order resonance of the cavity ($\lambda_{AO}/2$). The solid grey line tracks the trend of the simulated signal peak, in agreement with theory, and clearly deviates from $\lambda_{AO}/2$. The dark signal in the experiments that appears immediately below the resonance is due to the use of a homodyne measurement technique (Supplementary Section 5.4). **c**, Measured phase (taken with PsHet scattering-type SNOM) as a function of cavity width for cavity N1 (25-nm-thick hBN flake), showing a π -phase jump across the resonance.

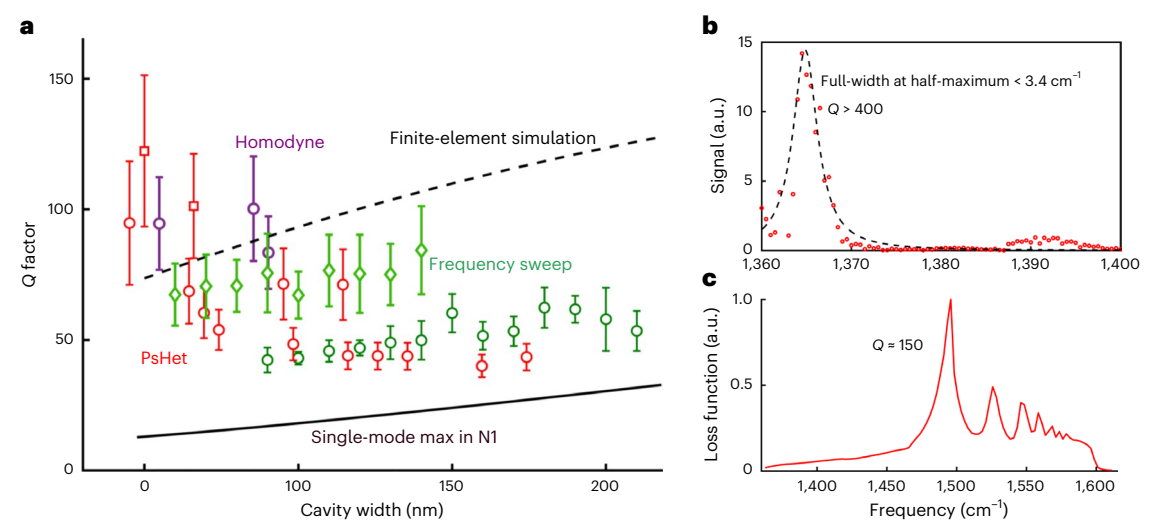


Fig. 3 | **Quality of confinement in nanocavities. a**, Measured Q factor versus cavity width, for different sets of cavities, N1 (indicated by circles), N2 (squares) and H2 (diamonds). The measured values have been extracted by different types of measurement: frequency sweeps (green), fourth-harmonic PsHet scans (red) and fourth-harmonic homodyne amplitude scans (purple). The dashed black line is a finite-element simulation for a 25-nm-thick 11 B hBN flake, similar to cavity set N1. The solid black line shows the calculated single-mode upper-bound limit, obtained without multimodal effects. This calculation is made using the experimentally measured PhP wavelengths for N1. Supplementary Section 2.3 shows a similar single-mode calculation for N2 and H2. Device H1 is not shown

here, since multimodal enhancement cannot be experimentally distinguished when the resonance bandwidth is so narrow and the Q factor approaches the absorption limit. Curiously, experiments show an increase in Q when the cavity width shrinks, in contrast to finite-element simulations, which could be related to improved structural quality (Supplementary Section 5.8). **b**, Response spectrum of a large $600 \times 600 \text{ nm}^2$ cavity in the H1 set (red dots, fourth-harmonic homodyne). The dashed black line shows a Lorentzian fit of the first cavity mode with a narrow linewidth corresponding to $Q \approx 480$. **c**, Semi-analytical calculation of the loss function 48 in a 100-nm-wide trench cavity, made with a 25-nm-thick flake.

With the exception of cavity set H1, the Q factor of our cavities is well below the absorption-limited Q factor (698 or 826, depending on the boron isotope), implying that confinement is exclusively limited by leakage. Theoretically, one can estimate the amount of leakage in a single-mode model based on the impedance mismatch between the relatively low-momentum mode of PhPs inside the cavity and the higher PhP momentum on the gold substrate outside (Supplementary Sections 2.2 and 2.3 provide the detailed calculations). Remarkably, the experimentally measured Q factors (in sets N1, N2 and H2) exceed the upper bound on the Q factor predicted in this single-mode model (Fig. 3a). Likewise, finite-element simulations (Fig. 3a) and a semi-analytical model of the one-dimensional cavity ⁴⁸ (Fig. 3c) also

yield *Q* factors far above the single-mode maximum. This points at the importance of multimodal physics in the confinement mechanism.

We can draw a similar conclusion from a control experiment performed with a 'counter example cavity'—an inverted design where the hBN lies on a metallic patch that is surrounded by a dielectric (SiN) substrate, instead of a dielectric patch (hole) surrounded by metal. If only a single PhP mode exists in the cavity, the inverted cavity should support impedance-mismatch resonances with a *Q* factor similar to the regular (MEC) cavities. Figure 4a shows the SNOM signal measured from the inverted cavity, which is much weaker, more localized and has a distinct cross-like shape that distinguishes it from the cavity resonance in the MEC (Fig. 4a and Supplementary Section 5.7). As observed in the

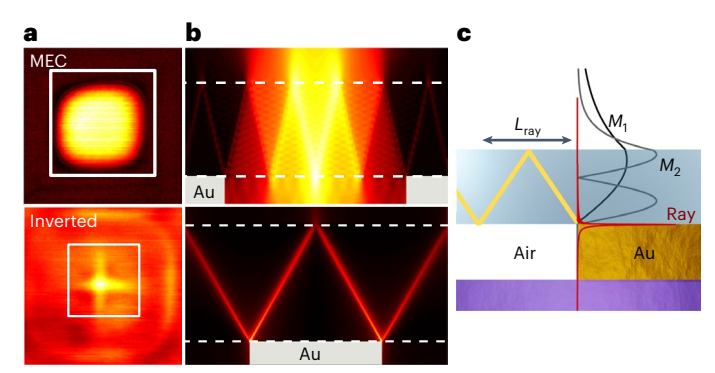


Fig. 4 | Multimodal reflection. a, Fourth-harmonic signal of a SNOM measurement (homodyne) of a resonant 600 × 600 nm² MEC cavity (top; $f = 1,368 \text{ cm}^{-1}$) and an inverted cavity, $300 \times 300 \text{ nm}^2 \text{ sized}$, (bottom; $f=1,381 \,\mathrm{cm}^{-1}$) at their respective expected resonant frequencies. The MEC shows a clear resonant state with practically no visible leakage. The inverted cavity shows no clear resonance. The relatively weak signal in the middle of the cavity is associated with launching from the cavity corners. The brighter areas in the colour map correspond to a higher signal and each subplot is separately normalized. b, Simulated electric-field cross-section of an MEC cavity (top; $f = 1,497 \text{ cm}^{-1}$) and an inverted cavity (bottom; $f = 1,393 \text{ cm}^{-1}$). The MEC cavity resonance shows ray-like features and undulations with a wavelength associated with higher-order modes. In contrast, the inverted cavity is not resonant, since the multimodal-ray excitations can freely escape it. Supplementary Section 4.2 and Supplementary Videos 1-5 show the additional frequencies and details. The simulation dimensions are scaled for presentation purposes, the size of the MEC (inverted cavity) is 260 nm and the flake is 10 nm thin. The colour bar is identical to the one shown in Fig. 2b. c, Illustration of nanoray reflection. A ray, with an L_{ray} skip distance, is incident on the metallic corner of the cavity. The calculated nanoray-field profile (red line) has minimal overlap with the M_1, M_2 PhP modes (black and grey lines, respectively) on the metal substrate, leading to enhanced reflection.

accompanying simulations (Fig. 4b and Supplementary Section 4.2), this weaker signal is the result of non-resonant PhP launching from the corners of the cavity. Thus, for the inverted cavity, the presence of additional modes substantially reduces the confinement quality, in sharp contrast with our findings for MECs.

To understand the physical mechanism of enhancement in our MECs, we first consider the basic excitation of a hyperbolic medium: although the eigenmodes of a hyperbolic metamaterial slab are delocalized, placing a dipole source on the slab excites a superposition of the eigenmodes in the slab (Fig. 4b, A_0 , A_1 ...). This superposition forms a transverse-magnetic-polarized ray-like excitation whose electric field is strongly concentrated in a narrow nanoscale ray⁴⁹. This ray propagates at a fixed angle of $\pm atan\left(\operatorname{Re}\left(\sqrt{-\epsilon_{x}/\epsilon_{z}}\right)\right)$ inside the flake, performing a zig-zag motion between the top and bottom interface. Unlike optical beams more commonly encountered in optics, this ray does not continuously accumulate phase, but through discrete reflection events, whenever the ray is mirrored off the top or bottom of the flake. As it propagates, the nanoray also absorption-broadens as $\Gamma \simeq \operatorname{Im} \left(\sqrt{-\epsilon_x/\epsilon_z} \right) x$, which—for our experimental parameters—is about 1-2 nm in a flake with a thickness of t = 25 nm. Enhanced backreflection (such that the ray propagates backwards along the path of the incoming ray) will occur if this nanoray is incident on the sharp (nanometrescale) corner of a metallic structure. Above a metallic substrate, the electric field of the eigenmodes M_1, M_2 ... is zero at the hBN-metal interface due to screening (Fig. 4c). Therefore, the overlap of the narrow ray with any of the modes on the metal is very small and the reflection can approach unity for $t \gg \Gamma(\text{ref.} 49)$. Importantly, this reflection enhancement effect is inherently asymmetric—a beam incident on the corner from the metal substrate side will not experience this enhancement. In fact, it experiences a counterpart effect of transmission enhancement, as is evident from our results with the inverse cavity (Fig. 4a,b, bottom).

To demonstrate how enhanced multimodal rays are reflected, we simulated the intensity profile of a ray generated by a dipole source as it propagates in an hBN flake in the vicinity of a sharp metallic corner (Fig. 1d and Supplementary Videos 1-5). When the ray is precisely incident on the metallic corner, it is strongly reflected with an estimated power reflection coefficient of 93%. If we slightly shift the dipole frequency (4 cm⁻¹), the angle of propagation of the multimodal ray changes and the ray hits ~10 nm after the metallic corner (that is, a distance several times the ray thickness). Since the ray misses the metallic corner, it is transmitted almost perfectly; hence, its reflection is reduced rather than enhanced by multimodal interference, similar to the reduced Q factor observed in the inverted cavity. Likewise, smoothening the cavity corners reduces the effectiveness of the ray reflection mechanism and reduces the MEC Q factor (Supplementary Section 4.1). We emphasize that confinement in an MEC cavity occurs due to a combination of multimodal effects and more simple impedance-mismatch mechanisms. Higher-order modes decay faster than lower-order modes in the cavity and are less efficiently excited in the cavity due to their larger momentum. Hence, the multimodal ray broadens due to absorption as it propagates inside the cavity. After circulating in the cavity, only the first few modes $(A_0, A_1 \text{ and } A_2)$ play a role and eventually there is only one mode in the cavity and the reflection mechanism is more similar to impedance mismatch.

In practice, the magnitude of multimodal reflection enhancement we have in our experiments is restricted, due to both absorption (which broadens the width of the ray and diminishes the strength of the reflection mechanism) and smearing of the effect by the finite size of the scattering-type SNOM tip and its distance above the hBN. This is most evident when comparing the simulations shown in Fig. 2b, which simulate a finite semi-spherical tip and additional simulations (Supplementary Section 5) where light is coupled into the cavity via an infinitesimally sharp element. In the latter case, the cavity response and Q factor increase whenever the ray completes an integer number of bounces inside the cavity. For the finite-tip-size simulation, a modulation with the cavity size is seen, but is much less pronounced. In the experiment, such a modulation is hard to recognize, suggesting that the effect is even further smeared out. In particular, all the Q factors in the calculation, simulations and experiment exceed the single-mode limit.

To conclude, we return to the data shown in Fig. 1a and compare our MEC resonators in the current work with all the other types of nanocavity. For Q = 50-100, our MEC cavities are orders of magnitude smaller than any other optical resonator of a comparable Q, in terms of both absolute volume and normalized volume. This high Q (low loss) is a testament to the power of our MEC approach and to the power of indirect patterning, which can be elegantly applied to assemble a range of nanoscale devices. Moreover, the small volume of our cavities implies a gigantic Purcell enhancement of $Q/V \gg 10^8 \lambda_0^{-3}$, making it a unique platform to study material systems as well as to modify their behaviours via light-matter interaction⁵⁻¹⁴. Future prospects for our $work \, include \, using \, hBN \, nanotubes^{40}, instead \, of \, hBN \, flakes, in \, the \, hopes \, and \, he \, hopes \, are the include a constant of th$ of achieving an even larger degree of confinement and Purcell enhancement. Alternatively, many of the insights of our work can be applied to artificial hyperbolic metamaterial cavities, thereby creating higher-quality cavities in the near-infrared or visible parts of the spectrum.

Online content

Any methods, additional references, Nature Portfolio reporting summaries, source data, extended data, supplementary information, acknowledgements, peer review information; details of author contributions and competing interests; and statements of data and code availability are available at https://doi.org/10.1038/s41563-023-01785-w.

References

- Baumberg, J. J. et al. Extreme nanophotonics from ultrathin metallic gaps. Nat. Mater. 18, 668–678 (2019).
- Chikkaraddy, R. et al. Single-molecule strong coupling at room temperature in plasmonic nanocavities. *Nature* 535, 127–130 (2016).
- 3. Benz, F. et al. Single-molecule optomechanics in 'picocavities'. Science **354**, 726–729 (2016).
- Leng, H. et al. Strong coupling and induced transparency at room temperature with single quantum dots and gap plasmons. Nat. Commun. 9, 4012 (2018).
- Yoo, D. et al. Ultrastrong plasmon-phonon coupling via epsilon-near-zero nanocavities. Nat. Photon. 15, 125–130 (2021).
- Mueller, N. S. et al. Deep strong light-matter coupling in plasmonic nanoparticle crystals. *Nature* 583, 780–784 (2020).
- Ciuti, C., Bastard, G. & Carusotto, I. Quantum vacuum properties of the intersubband cavity polariton field. *Phys. Rev. B* 72, 115303 (2005).
- Frisk Kockum, A. et al. Ultrastrong coupling between light and matter. Nat. Rev. Phys. 1, 19–40 (2019).
- Andolina, G. M., Pellegrino, F. M. D., Giovannetti, V., MacDonald, A. H. & Polini, M. Theory of photon condensation in a spatially varying electromagnetic field. *Phys. Rev. B* 102, 125137 (2020).
- Schäfer, C., Flick, J., Ronca, E., Narang, P. & Rubio, A. Shining light on the microscopic resonant mechanism responsible for cavity-mediated chemical reactivity. *Nat. Commun.* 13, 7817 (2022).
- Schuller, J. et al. Plasmonics for extreme light concentration and manipulation. *Nat. Mater.* 9, 193–204 (2010).
- 12. Ashida, Y., İmamoğlu, A. & Demler, E. Cavity quantum electrodynamics with hyperbolic van der Waals materials. *Phys. Rev. Lett.* **130**, 216901 (2023).
- Flick, J., Ruggenthaler, M., Appel, H. & Rubio, A. Atoms and molecules in cavities, from weak to strong coupling in quantum-electrodynamics (QED) chemistry. *Proc. Natl Acad. Sci.* USA 114, 3026–3034 (2017).
- Garcia-Vidal, F. J., Ciuti, C. & Ebbesen, T. W. Manipulating matter by strong coupling to vacuum fields. Science 373, eabd0336 (2021).
- Santhosh, K. et al. Vacuum Rabi splitting in a plasmonic cavity at the single quantum emitter limit. Nat. Commun. 7, ncomms11823 (2016).
- Kuttge, M., García De Abajo, F. J. & Polman, A. Ultrasmall mode volume plasmonic nanodisk resonators. *Nano Lett.* 10, 1537–1541 (2010).
- Epstein, I. et al. Far-field excitation of single graphene plasmon cavities with ultracompressed mode volumes. Science 368, 1219–1223 (2020).
- Brar, V. W. et al. Highly confined tunable mid-infrared plasmonics in graphene nanoresonators. Nano Lett. 13, 2541–2547 (2013).
- Nikitin, A. et al. Real-space mapping of tailored sheet and edge plasmons in graphene nanoresonators. *Nat. Photon.* 10, 239–243 (2016).
- Wang, S. et al. Metallic carbon nanotube nanocavities as ultracompact and low-loss Fabry-Pérot plasmonic resonators. Nano Lett. 20, 2695–2702 (2020).
- Mock, J. J. et al. Shape effects in plasmon resonance of individual colloidal silver nanoparticles. J. Chem. Phys. 116, 6755–6759 (2002).
- Kelly, K. L. et al. The optical properties of metal nanoparticles: the influence of size, shape, and dielectric environment. *J. Phys. Chem. B* 107, 668–677 (2003).
- Yang, X. et al. Experimental realization of three-dimensional indefinite cavities at the nanoscale with anomalous scaling laws. Nat. Photon. 6, 450–454 (2012).

- Indukuri, S. C. et al. Ultrasmall mode volume hyperbolic nanocavities for enhanced light–matter interaction at the nanoscale. ACS Nano 13, 11770–11780 (2019).
- Dubrovkin, A. M. et al. Resonant nanostructures for highly confined and ultra-sensitive surface phonon-polaritons. Nat. Commun. 11, 1863 (2020).
- Wang, T. et al. Optical properties of single infrared resonant circular microcavities for surface phonon polaritons. *Nano Lett.* 13, 5051–5055 (2013).
- Alfaro-Mozaz, F. et al. Nanoimaging of resonating hyperbolic polaritons in linear boron nitride antennas. *Nat. Commun.* 8, 15624 (2017).
- Giles, A. J. et al. Imaging of anomalous internal reflections of hyperbolic phonon-polaritons in hexagonal boron nitride. Nano Lett. 16, 3858–3865 (2016).
- Ambrosio, A. et al. Mechanical detection and imaging of hyperbolic phonon polaritons in hexagonal boron nitride. ACS Nano 11, 8741–8746 (2017).
- 30. Tamagnone, M. et al. Ultra-confined mid-infrared resonant phonon polaritons in van der Waals nanostructures. Sci. Adv. 4, eaat7189 (2018).
- Tamagnone, M. et al. High quality factor polariton resonators using van der Waals materials. Preprint at https://arxiv.org/ abs/1905.02177 (2019).
- 32. Autore, M. et al. Boron nitride nanoresonators for phonon-enhanced molecular vibrational spectroscopy at the strong coupling limit. *Light Sci. Appl.* **7**, 17172 (2018).
- 33. Caldwell, J. et al. Sub-diffraction, volume-confined polaritons in the natural hyperbolic material, hexagonal boron nitride. *Nat. Commun.* **5**, 5221 (2014).
- Brown, L. V. et al. Nanoscale mapping and spectroscopy of nonradiative hyperbolic modes in hexagonal boron nitride nanostructures. *Nano Lett.* 18, 1628–1636 (2018).
- Autore, M., Dolado, I. & Li, P. Enhanced light–matter interaction in ¹⁰B monoisotopic boron nitride infrared nanoresonators. *Adv. Opt. Mater.* 9, 2001958 (2021).
- Yang, J. et al. Ultrasmall metal-insulator-metal nanoresonators: impact of slow-wave effects on the quality factor. Opt. Express 20, 16880–16891 (2012).
- Chatzakis, I. et al. Strong confinement of optical fields using localized surface phonon polaritons in cubic boron nitride. Opt. Lett. 43. 2177–2180 (2018).
- Lee, I. H. et al. Image polaritons in boron nitride for extreme polariton confinement with low losses. *Nat. Commun.* 11, 3649 (2020).
- 39. Giles, A. et al. Ultralow-loss polaritons in isotopically pure boron nitride. *Nat. Mater.* **17**, 134–139 (2018).
- 40. Guo, X. et al. Hyperbolic whispering-gallery phonon polaritons in boron nitride nanotubes. *Nat. Nanotechnol.* **18**, 529–534 (2023).
- 41. Duan, J. et al. Active and passive tuning of ultranarrow resonances in polaritonic nanoantennas. *Adv. Mater.* **34**, 2104954 (2022).
- Low, T. et al. Polaritons in layered two-dimensional materials. Nat. Mater. 16, 182–194 (2017).
- Ocelic, N., Huber, A. & Hillenbrand, R. Pseudoheterodyne detection for background-free near-field spectroscopy. Appl. Phys. Lett. 89, 101124 (2006).
- 44. Hillenbrand, R. et al. Coherent imaging of nanoscale plasmon patterns with a carbon nanotube optical probe. *Appl. Phys. Lett.* **83**, 368–370 (2003).
- 45. Li, P. et al. Hyperbolic phonon-polaritons in boron nitride for near-field optical imaging and focusing. *Nat. Commun.* **6**, 7507
- Dai, S. et al. Subdiffractional focusing and guiding of polaritonic rays in a natural hyperbolic material. *Nat. Commun.* 6, 6963 (2015).

- 47. Li, N. et al. Direct observation of highly confined phonon polaritons in suspended monolayer hexagonal boron nitride. *Nat. Mater.* **20**, 43–48 (2020).
- 48. Torre, I., Orsini, L., Ceccanti, M., Herzig Sheinfux, H. & Koppens, F. H. L. Green's functions theory of nanophotonic cavities with hyperbolic materials. Preprint at https://arxiv.org/abs/2104.00511 (2021).
- Herzig Sheinfux, H. et al. Evolution and reflection of ray-like excitations in hyperbolic dispersion media. Preprint at https://arxiv.org/abs/2104.00091 (2021).

Publisher's note Springer Nature remains neutral with regard to jurisdictional claims in published maps and institutional affiliations.

Springer Nature or its licensor (e.g. a society or other partner) holds exclusive rights to this article under a publishing agreement with the author(s) or other rightsholder(s); author self-archiving of the accepted manuscript version of this article is solely governed by the terms of such publishing agreement and applicable law.

© The Author(s), under exclusive licence to Springer Nature Limited 2024

Methods

Supplementary Information provides detailed methods and extended discussion of the techniques.

Sample fabrication

The cavity substrate for N1 and N2 is a Si chip with a 285 nm SiO₂ oxide layer on which a metallic layer of 2 nm Cu is sputtered, followed by an evaporated 10 nm Au (Kurt J. Lesker Company-LAB 18 thin-film deposition system). The resulting gold layer is ultraflat with a less than 0.5 nm root mean square roughness. For cavity sets H1 and H2, the substrate is a commercial 20-nm-thick SiN membrane (Norcada), evaporated in the same manner. The metallic surface is patterned using a Ne⁺ (He⁺) FIB (Zeiss Orion microscope), which is focused to a spot size of ~6 nm (~2 nm), working with 5 uT gas pressure and a 10 um aperture. Isotopically pure hBN flakes are then mechanically exfoliated and transferred onto the substrate using one of two standard techniques (Supplementary Sections 3.3 and 3.4 provide additional details). Cavities C1, H1 and H2 and the large trench are made using polydimethylsiloxane-based exfoliation and transfer (XO retention, DGL type from Gelpak). Cavity N2 was made with a polycarbonate transfer, using home-made polycarbonate stamps. Contact-mode atomic force microscopy (AFM) was used to clean the surface of cavity sets N1 and N2. We emphasize that both the quality of the flakes and high FIB resolution were shown to be instrumental to the success of the measurements reported here and we, therefore, provide additional detail on the fabrication process (Supplementary Section 3).

The inverse cavity was made starting with a 20-nm-thick SiN membrane and evaporating a 10 nm layer of gold on the underside of the membrane (for grounding purposes). Through holes were milled using Ne FIB (holes confirmed to be through in the AFM data). An hBN flake was transferred (by polydimethylsiloxane) on the top side of the membrane, followed by a second round of evaporation on the membrane underside. The gold, hence, fills the holes in the membrane, creating topographically flat patches of gold substrate underneath the hBN (flatness confirmed by the AFM data).

Near-field measurements

All the measurements were performed using a commercially available scattering-type near-field microscope (neaspec), equipped with Pt-coated AFM tips (Arrow NCPt from NanoAndMore; nominal diameter, 40–50 nm). The laser source was a tunable quantum cascade laser (Daylight Instruments MIRcat), giving 10 to 90 mW continuous-wave laser power, depending on the frequency. In the homodyne mode, the laser frequency was increased in small increments using a computerized interface to produce frequency sweeps and the signal at each frequency was normalized against the maximum signal measured far away from the cavities, during the exact same scan. Such high-resolution frequency scans are sensitive to mechanical (piezo) drift, the exact amount of which changes from measurement to measurement and which prevents the measurement of smaller cavities. As an alternative, two-dimensional measurements with a lower spectral resolution are also possible, in which case the frequency response can be extracted (Supplementary Section 5).

Theoretical analysis

Supplementary Information provides details on the theory on the formation of bound in the continuum modes and the evaluation of cavities on a single-mode basis. Numerical calculation of ray propagation and reflection were made with Lumerical, the cavity SNOM response was simulated using COMSOL Multiphysics and the cavity response was simulated using a rigorous coupled-wave approach. In addition, a semi-analytical approach was used to calculate the cavity modes as well as to confirm that the cavity-mode volume is very similar to the cavity volume.

Data availability

The data that support the findings of this study are available from the corresponding author upon request.

Acknowledgements

F.H.L.K. acknowledges support from the ERC TOPONANOP under grant agreement no. 726001, the ERC proof-of-concept grant Polarsense, the Government of Spain (FIS2016-81044; Severo Ochoa CEX2019-000910-S), Fundació Cellex, Fundació Mir-Puig and Generalitat de Catalunya (CERCA, AGAUR, SGR 1656). Furthermore, the research leading to these results has received funding from the European Union's Horizon 2020 programme under grant agreement no. 881603 (Graphene Flagship Core3). H.H.S. acknowledges funding from the European Union's Horizon 2020 programme under the Marie Skłodowska-Curie grant agreement no. 843830. N.C.H.H. acknowledges funding from the European Union's Horizon 2020 programme under the Marie Skłodowska-Curie grant agreement no. 665884. R.B. acknowledges funding from the European Union's Horizon 2020 research and innovation programme under the Marie Skłodowska-Curie grant agreement no. 847517. L.O. acknowledges support by The Secretaria d'Universitats i Recerca del Departament d'Empresa i Coneixement de la Generalitat de Catalunya, as well as the European Social Fund (L'FSE inverteix en el teu futur)—FEDER. M.C. acknowledge the support of the 'Presencia de la Agencia Estatal de Investigación' within the Convocatoria de tramitación anticipada, correspondente al año 2020, de las ayudas para contractos predoctorales (Ref. PRE2020-094864) para la formación de doctores contemplada en el Subprograma Estatal de Fromación del Programa Estatal de Promoción del Talento y su Empleabilidad en I+D+i, en el marco del Plan Estatal de Investigacón Científica y Técnica de Innovación 2017-2020, cofinanciado por el Fondo Social Europeo. J.H.E. acknowledges support from the Office of Naval Research (award NOO014-20-1-2474). M.J. and G.S. acknowledge support from the Office of Naval Research (ONR) under grant no. N00014-21-1-2056, the support of the Army Research Office under award W911NF2110180 and by the National Science Foundation (NSF) under grant no. DMR-1719875. M.J. was also supported in part by the Kwanjeong Fellowship from Kwanjeong Educational Foundation. R.M. and V.P. acknowledge support from the Opto group Plan Nacional project (TUNASURF). We also wish to thank J. Osmond, H. Lozano and N. V. Hulst for help with the FIB operation, which was also supported by the European Commission under ERC Advanced Grant 670949-LightNet.

Author contributions

H.H.S., L.O., M.C., D.B.R., S.C., R.M. and V.P. worked on the sample fabrication with help from A.Hötger. and A.Holleitner. The isotopic hBN crystals were grown by E.J. and J.H.E. The measurements were performed by H.H.S. and L.O. with help from D.B.R. and N.C.H.H. The analytical and semi-analytical theory was developed by H.H.S., I.T. and M.C., and the numerical calculations were performed by M.J., M.C., S.M., R.B. and G.S. The experiments were designed by H.H.S. and F.H.L.K. All authors contributed to writing the manuscript and A.Holleitner., V.P., G.S. and F.H.L.K. supervised the work.

Competing interests

The authors declare no competing interests.

Additional information

Supplementary information The online version contains supplementary material available at https://doi.org/10.1038/s41563-023-01785-w.

Correspondence and requests for materials should be addressed to Frank H. L. Koppens.

Peer review information *Nature Materials* thanks the anonymous reviewers for their contribution to the peer review of this work.

Reprints and permissions information is available at www.nature.com/reprints.